Electronic Supplementary Material (ESI) for Journal of Materials Chemistry A.
This journal is © The Royal Society of Chemistry 2021

A bioinspired 3D solar evaporator with balanced water supply and evaporation for highly efficient photothermal steam generation

Yiming Bu [a], Yongheng Zhou[b], Weiwei Lei [a], Lipei Ren[b], Jinfeng Xiao[b], Hongjun Yang[b], Weilin Xu [b], Jingliang Li* [a]*

a. Institute for Frontier Materials, Deakin University, Geelong, Victoria 3216, Australia
b. Key Laboratory of Green Processing and Functional New Textile Materials of Ministry of Education, Wuhan Textile University, Wuhan 430200, P. R. China

*Corresponding author Email: h_j.yang@yahoo.com, jingliang.li@deakin.edu.au

1.1 Geometry Design of Evaporator

Maximizing light absorption is vital for achieving high-yield steam generation. In a macroscopic view, when light irradiates on the surface of a 2D plane material, reflected light cannot bounce back to the material, which means only a small portion of the incident light can be harvested. To reduce energy loss from reflectance, constructing concave structures on the surface of photothermal materials was a promising and effective strategy to harvest multiple reflections.[1, 2] Herein, a 3D conical structure was rationally designed to maximize the times of light reflections and absorption to improve the utilization of light. **Fig. S1a** schematically compares the light-harvesting property of a 2D plane surface and 3D conical structure, where incident light can be trapped inside the 3D CFC cone by simple diffuse reflection process, but only single reflection occurred on the surface of a 2D CF fabric. By reducing the angle of apex, most portion of incident light could be further absorbed by 3D conical structure due to multiple reflections occurred, which could be regarded as amplification of multi-absorption along with microstructures.[1, 3]

Based on the consideration that the critical sunlight incidence angle (α) (to the vertical) varies from 60 ° (sunrise at 8: 00 a.m.) to 0 ° (noon at 12: 00) then back to 60 ° (sunset at 4: 00 p.m.),[4] the apex of the 3D CFC-Cone evaporator was rationally designed as 60 ° (Fig. S1b). As the sun rises, the sunlight angle $\boldsymbol{\alpha}$ is less than 60 ° so that multiple internal reflections occur, where the incident beams firstly hit one side of the conical structure, then the light was reflected to other side, resulting in multiple light reflection and absorption, until the light is completely absorbed. This means that the elaborate 3D cone structure can effectively “trap” sunlights and maximize the use of incident sunlights, thereby excellent heat regulation system was built then photothermal conversion efficiency could be further improved.

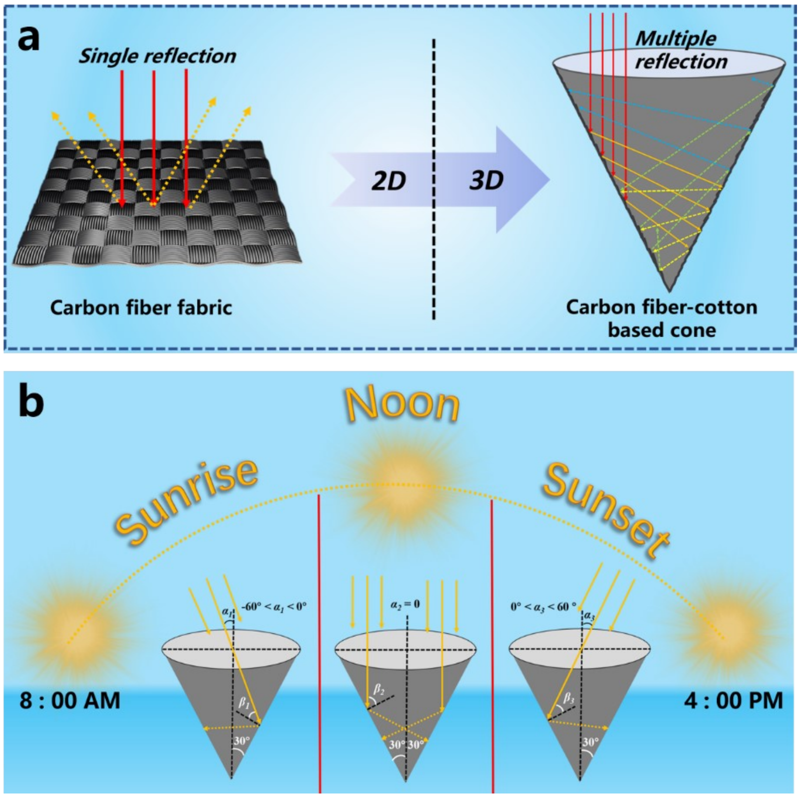

Fig. S1. a) Schematic illustration of light reflection process on 2D carbon fibre fabric and 3D CFC-Cone; b) Schematic illustration of light reflection process inside the 3D CFC-Cone with incident light irradiating from different angles.

1.2 Quantification of the 3D CFC-Cone Evaporator

To quantify the solar-driven steam generation performance, the solar-to-steam conversion efficiency (η) was calculated via equations (1) and (2).

$$\eta = \dot{m}\,(Lv + Q) \,/\, E_{in} \qquad (1)$$

$$Lv = 1.91846 \times 10^{6}\,[T_1/(T_1 - 33.91)]^2 \qquad (2)$$

where $\dot{m}$ (kg/m^{2}h) is the water evaporation rate under steady-state conditions ($\dot{m} = m_{Light} - m_{Dark}$), Lv is the total enthalpy of water vaporization (J kg^{-1}), Q is the sensible heat of water of unit mass [$Q = c\,(T_1 - T_0)$] (J kg^{-1}), c is the specific heat capacity of water (4.2 J g^{-1} K^{-1}), T_1 represents the average surface temperature for vaporization (35.3 °C for

CFC-Cone-7) of the cone, T_0 denotes the initial average surface temperature of the cone (24.2 °C) and E_{in} is the energy input of incident light (that is 1.0 kW m^{-2}).

The high efficiency was achieved by optimal design of the evaporator (cone configuration and optimal water supply paths) that maximized the light conversion efficiency, which is augmented by cold evaporation that harvested additional energy from the environment. According to the equations (1), (2) of solar-to-steam conversion efficiency (η) in ESI 1.2, assuming 100 % energy efficiency of solar-steam generation, the theoretical limit evaporation rate should be about 1.46 kg m^{-2} h^{-1}. In equation (1), the E_{in} is only the energy of incident light (a unit incident light energy of 1.0 kW m^{-2} was used in calculations), not including the additional energy gained from environment. In our work, when cold evaporation was present, the evaporation rate achieved was 3.27 kg m^{-2} h^{-1} and the efficiency of 194 % was obtained based on this evaporation rate using equation (1).

1.3 Numerical Simulation of Heat Transfer by COMSOL

Heat Transfer Module of Commercial COMSOL Multiphysic 5.5 was used to simulate the heat transfer process in 3D CFC-Cone, where the cotton bars were regarded as porous medium. The ray tracing module was used to simulate the absorption process of sunlight projected onto the surface of carbon fibre bundle, and the heat source distribution was obtained. The Darcy’s law was used to couple with the model of heat absorption in porous medium to restore the body temperature distribution of solar evaporator and the heat diffusion process.

$$A_jQ = (\rho C_P)_{eff} + \rho C_P\, u \cdot \nabla T + \nabla \cdot q \qquad (3)$$

$$q_{solar} = \frac{1}{Aj}\sum Qj \qquad (4)$$

$$q = -k_{eff} \nabla T + q_{solar} \quad (5)$$

$$(\rho C_P)_{eff} = \theta_p \rho_p C_{p,p} + (1-\theta_p)\, \rho C_P \quad (6)$$

$$k_{eff} = \theta_p k_p + (1-\theta_p)\, k \quad (7)$$

where A_j is the area of j finite element grid area (illuminated carbon fibre bundle area); Q represents heat flux (W m^{-3}); ρ represents the density of water; C_P denotes water heat capacity at a constant pressure; $(\rho C_P)_{eff}$ is the effective volumetric heat capacity of water at a constant pressure; ∇T is temperature gradient (K m^{-1}); q_{solar} is heat flux(W m^{-2}); Q_j is the energy of the photon received in the j finite element grid area (W); q denotes the heat flux vector (W m^{-2}); k_p (0.02 W m^{-2} K^{-1}) and k_{eff} represent the thermal conductivity and effective thermal conductivity (W m^{-1} K^{-1}) of the porous medium, respectively. Boundary conditions: Direct normal irradiance of similative solar light is 1000 W m^{-2} and number of rays are 10^6. u is the Darcy velocity (m s^{-1}), the velocity within the pores can be calculated as $u_L = u/\theta_p$, where θ_p represents the porosity of the material.

Porosity (θ_p) was assumed through equation (8) and (9), and this value was used in simulation.

$$\theta_p = \frac{v_1}{v_1 + v_0} \times 100\% \quad (8)$$

$$v_1 = \frac{m_{wet} - m_{dry}}{\rho} \quad (9)$$

where the v_1 is pore volume of 3D CFC-Cone; v_0 represents the absolute compact volume of 3D CFC-Cone which could be assumed by drainage method based on Archimedes Principle; m_{wet} is the weight of 3D CFC-Cone after absorbing full of water; m_{dry} is the weight of 3D CFC-Cone in a dry state; ρ is the density of water.

Darcy's velocity is the volume flow rate per unit cross sectional area. We used the Darcy flow module from COMSOL to simulate the flow of water in the evaporator. The governing equation for Darcy's quantification is as follows:

$$\nabla \cdot (\rho u) = Q_m \tag{10}$$

$$u = -\frac{\kappa}{\mu}\nabla p \tag{11}$$

where u is the Darcy's velocity; Q_m is the evaporation mass flow rate; κ is the permeability of the evaporator, which is obtained by the Kozeny-Carman model:

$$\kappa = \frac{d_p \quad \theta_p}{180(1-\theta_p)^2} \tag{12}$$

where d_p is the pore diameter, and θ_p is the porosity of 80%.

Table. 1 The parameters used in the simulation

Variable	Value	Describe
θ_p	0.8	Porosity
d_p	0.5 mm	Average pore diameter
k_p	0.02 W/m/K	Thermal conductivity of cotton
k_w	0.6 W/m/K	Thermal conductivity of water
k_c	10 W/m/K	Thermal conductivity of carbon fiber
h	5 W/m^2/K	External natural convection heat transfer coefficient
T_e	25°C	Environment temperature
T_0	20°C	Temperature of water

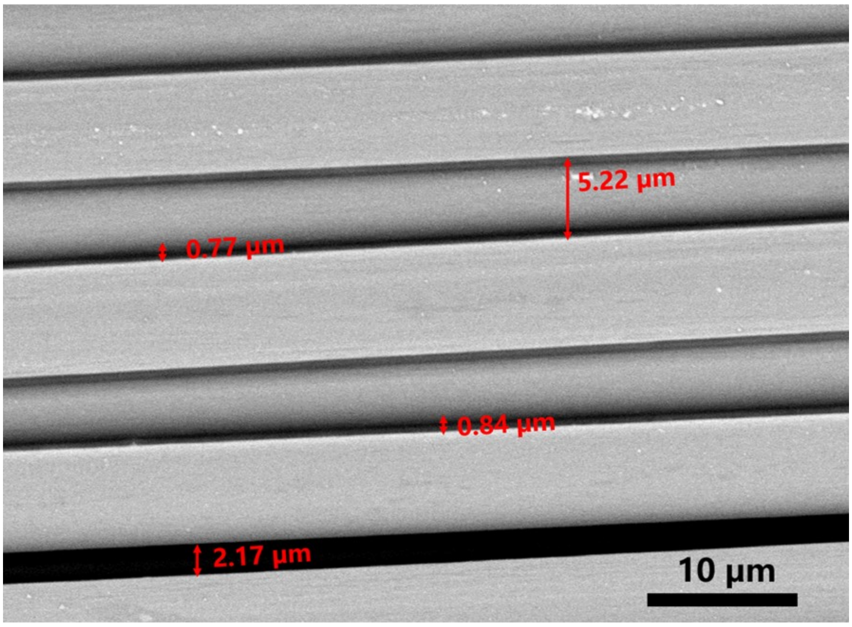

Fig. S2. The high magnification SEM image of carbon fibre bundle and the size of gap between individual single fibres.

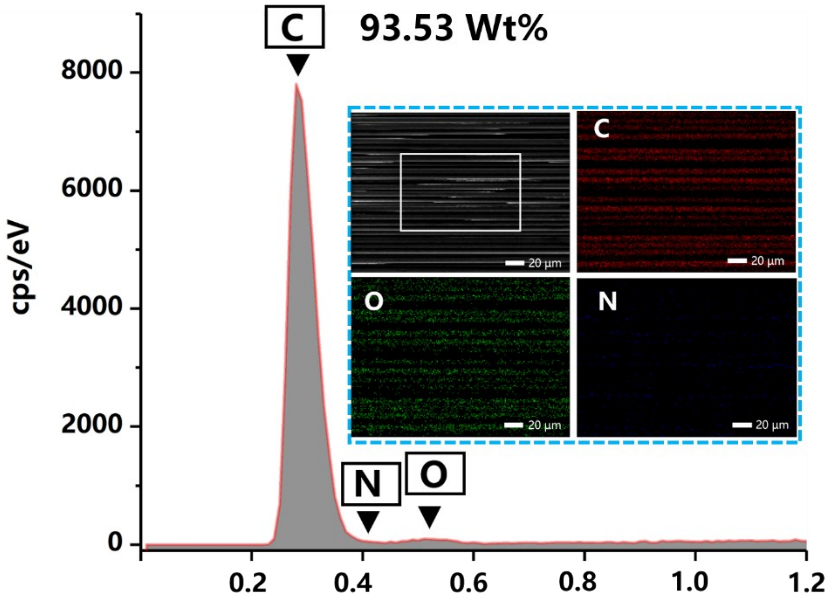

Fig. S3. Elemental composition (C, O and N) and mapping of carbon fibre bundle.

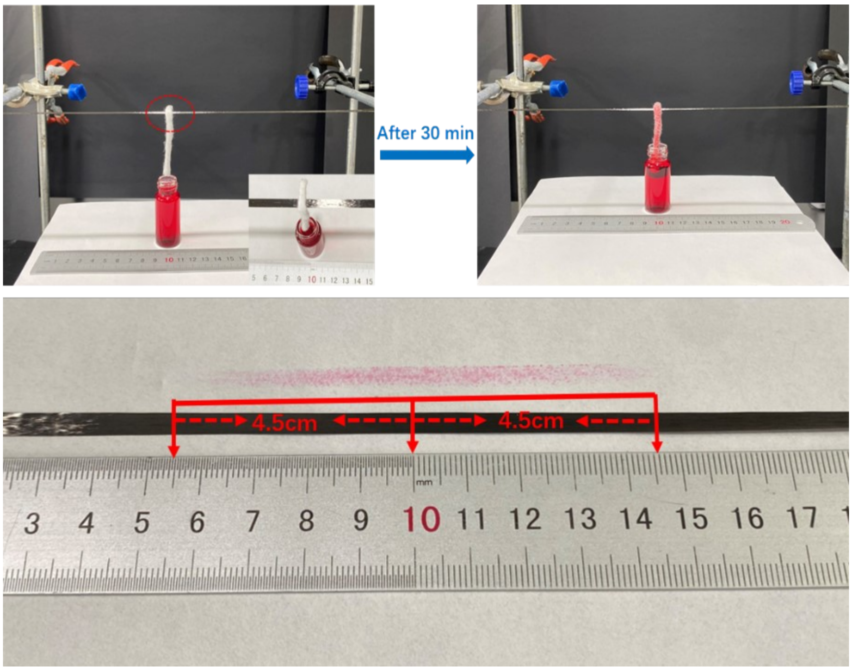

Fig. S4. A homemade setup for testing water transport in carbon fibre bundle.

A homemade setup was elaborately designed to verify water wicked in carbon fibre bundle, where cotton rod served as the water supply channel and water dyed red was used for tracing the water in the carbon fibre bundle. The carbon fibre bundle was wetted by water spreading out in the direction of aligned fibres leaving a red mark with a length 4.5 cm away from the middle after being pressed on a white paper, demonstrating that water could be transported in carbon fibre bundle owing to the capillary forces.

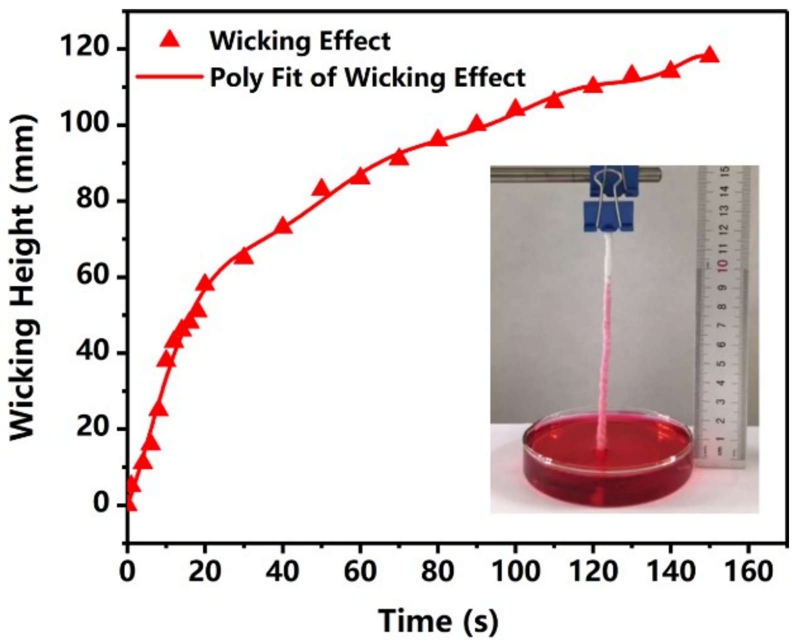

Fig. S5. The wicking rate of cotton rod.

The water supply flux of a single cotton bar was evaluated by measuring its water absorption at different time points during water transport from bottom to up. A single cotton bar enhanced by stainless steel with a height of 85.22 mm and diameter of 3.2 mm was fixed vertically, and its bottom was immersed in water for a certain time until it reached saturation state. The weight of a cotton bar before and after absorption of water at different time points were measured. The relationship between time and amount of water absorption per area was calculated by the method of linear regression. According to the above method, the water supply flux for 3D CFC-Cone-X could be obtained.

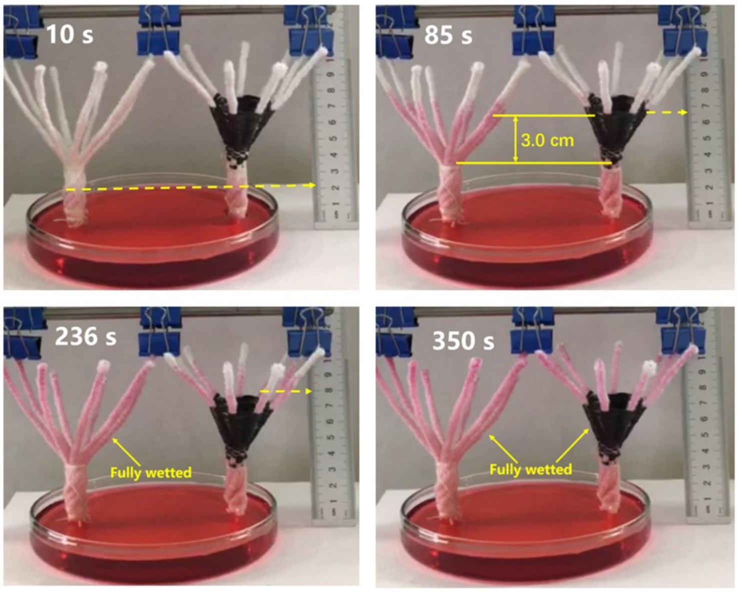

Fig. S6. Water wicking in conical frames.

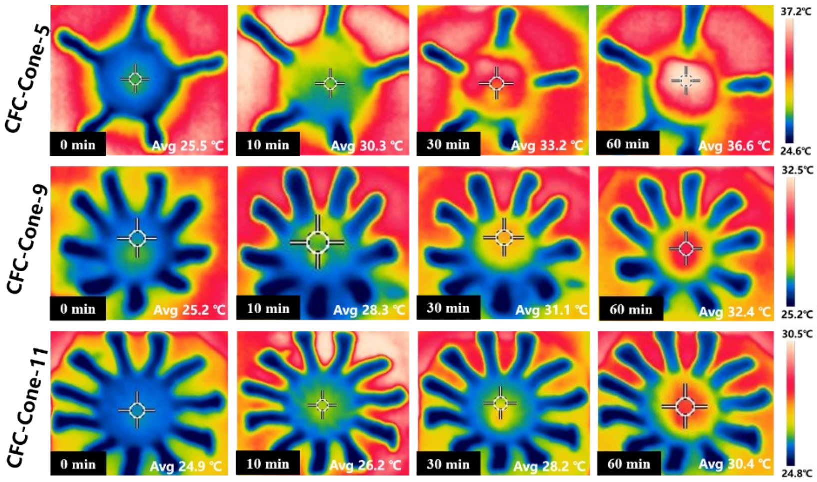

Fig. S7. Infrared images and time-dependent surface temperatures of 3D CFC-Cone evaporator with different number of cotton bars (5, 9 and 11).

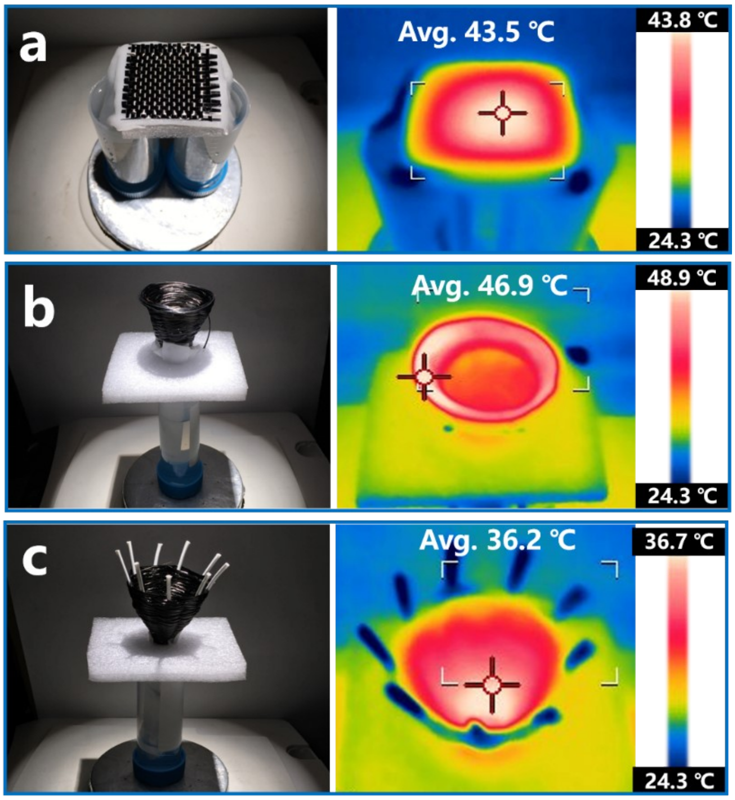

Fig. S8. Optical images of and IR image of (a) carbon fibre fabric, (b) 3D conical carbon fibre without water supply path, (c) 3D conical carbon fibre with PTFE hollow fibres as water supply path for water steam generation.

A 2D plane evaporator with a layer of carbon fibre fabric for photothermal conversion and a bottom layer of non-woven cotton fabric for water transport was fabricated and its performance was compared with another two weaved 3D conical evaporators with different ways for water supply. It is worth noting that such simple stack of 2D carbon fibre fabric and cotton could hardly keep them in close contact with each other so that the sufficient water supply could not be guaranteed. **Fig. S5a** shows that the surface temperature of carbon fibre fabric can reach 43.5 °C quickly which was higher that (35.6 °C) of 3D CFC-Cone-7 evaporator, but the evaporation rate (1.25 kg m^{-2} h^{-1}) of 2D evaporator was much lower than that of the 3D CFC cone evaporator (2.76 kg m^{-2} h^{-1}). The surface temperature (46.9 °C) of a 3D conical evaporator weaved by carbon fibre bundle without cotton bars as water supply channel was even higher than 2D carbon fibre fabric but evaporation rate could only reach 1.03 kg m^{-2} h^{-1} (**Fig. S5b**), where the extremely insufficient water supply flux could not keep pace with evaporation rate, thereby severely limiting evaporation rates. This further demonstrated the importance of sufficient water supply for solar-driven interfacial evaporators. In addition, hydrophilic PTFE hollow fibres were also used to enhance water transport in carbon fibre-based cone evaporator. However, only a slight increase in evaporation rate (1.35 kg m^{-2} h^{-1}) was achieved and the surface temperature was reduced to 36.2 °C (**Fig. S5c**), which could still be attributed to the insufficient water supply by PTFE hollow fibres.[5] Such scenarios indicated that system water evaporation rate was not simply proportional to the surface temperature. This could be due to the energy mismatch between heat converted from input solar light and the energy demanded for water evaporation, which could be regulated by tailoring the water supply amount around photothermal layer (irrespective of light-absorbing performance). Too much water supply would destroy the moderate thin water film that would become interfacial reservoir which absorb heat so that the surface temperature is reduced. On the other hand, insufficient water supply would lead to partial overheating along with heat loss but low water evaporation rate. Thus, balancing interfacial water supply and the surface temperature that related to water evaporation rate is a promising way to improve water generation rate.

Fig. S9. Optical image of vapor generating from CFC-Cone-5.

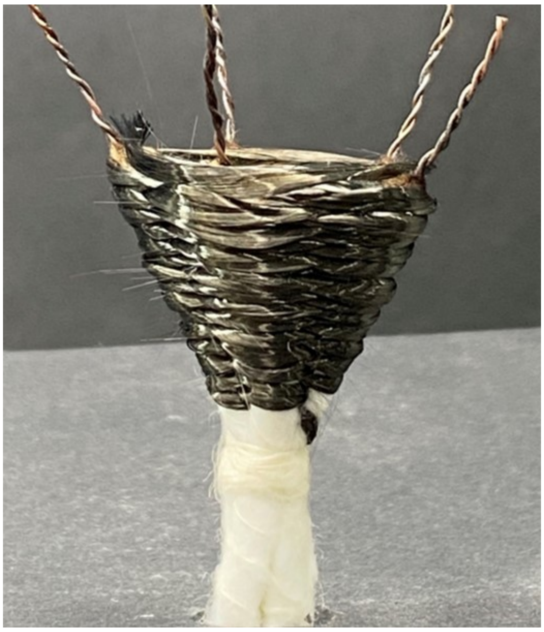

Fig. S10. Optical image of 3D CFC-Cone without upper cotton rods.

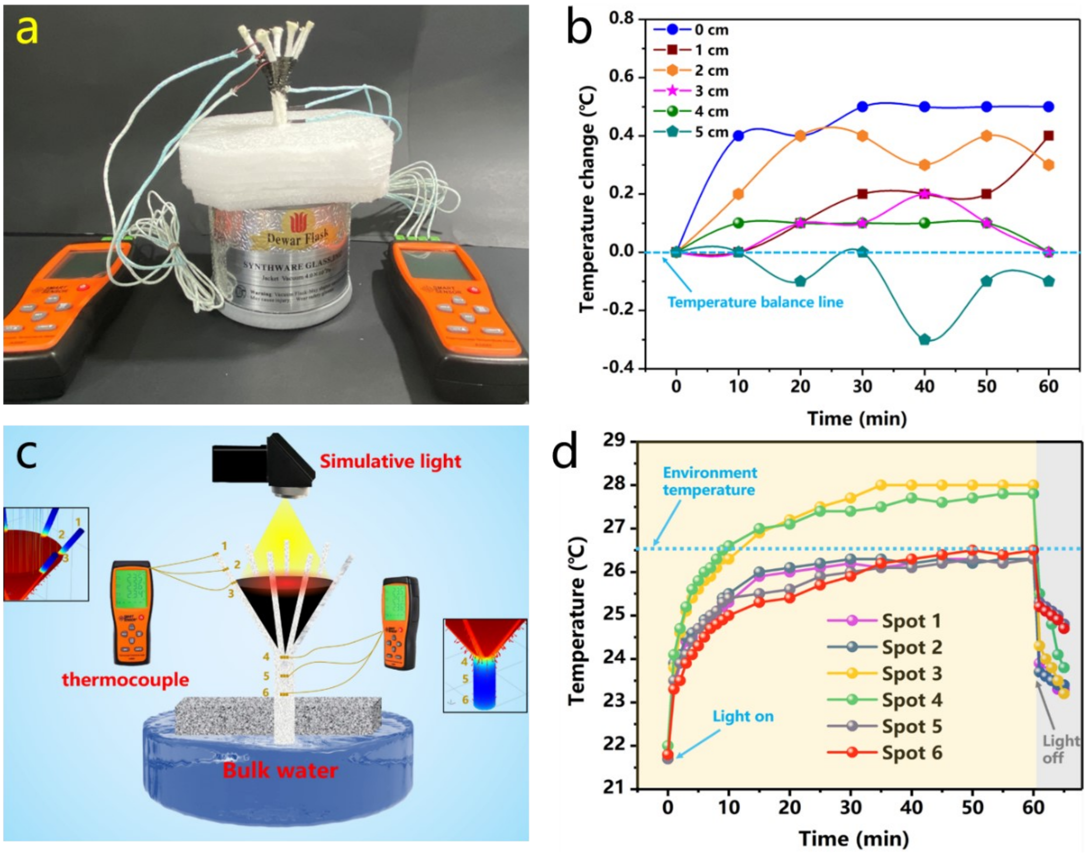

Fig. S11. (a) Optical image of 3D CFC-Cone-7-3 with thermocouples in branch cotton bars, rod and bulk water in Dewar flask; (b) Temperature change of bulk water for 3D CFC-Cone-7 with different heights of cotton rod (0-5 cm); (c) Diagram of three different parts of branch cotton bars and trunk rod of 3D CFC-Cone-7-3 monitored by thermocouples; (d) Surface temperature of different spots.

To analyze the mechanism of the energy distribution on the two cold evaporation parts (up and down, illustrated in **Fig. S8**) of 3D CFC-Cone-7-3, real-time surface temperature of different parts of 3D CFC-Cone was monitored by thermocouple sensor probes that were uniformly placed inside a up brunch cotton bar denoted as spots 1, 2, 3 and another three in trunk cotton rod as spot 4, 5, 6 (**Fig. S8c**). Time-dependent temperature change curve was plotted in **Fig. S8d**. Spot 3 and spot 4 show the highest equilibrium temperature, where energy was conducted upward and downward respectively. Two direction energy flow and the temperature deficit drove cold evaporation in two parts. After one hour illumination, equilibrium temperatures of other rest spots were almost equal to environment temperature, indicating that during the whole evaporation process, up and down cold evaporation area (7 branch cotton bars and trunk cotton rod) gained energy from environment to the greatest extent and consumed conductive heat loss from photothermal layer totally, thus leading to an extremely high evaporation rate of 3D CFC-Cone-7-3, which is 1.7 times higher than that of control one (1.93 kg m^{-2} h^{-1}, without any cold evaporation).

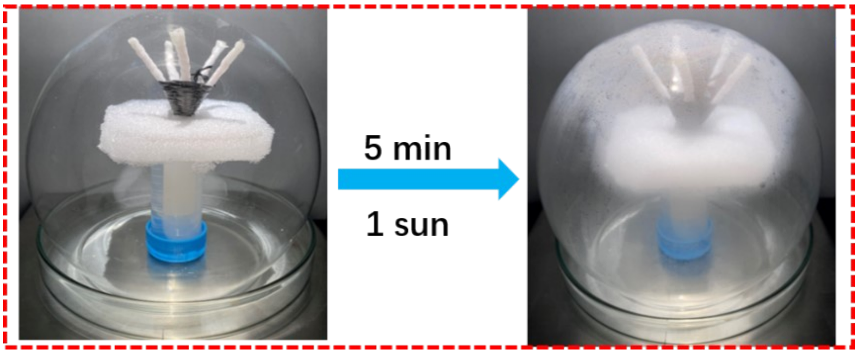

Fig. S12. Optical image 3D CFC-Cone-5 for water steam collection.

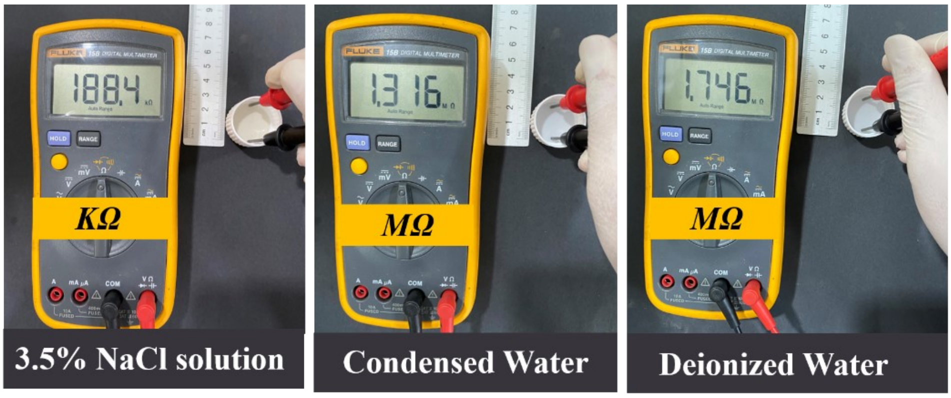

Fig. S13. Evaluation of desalination performance through a resistance test.

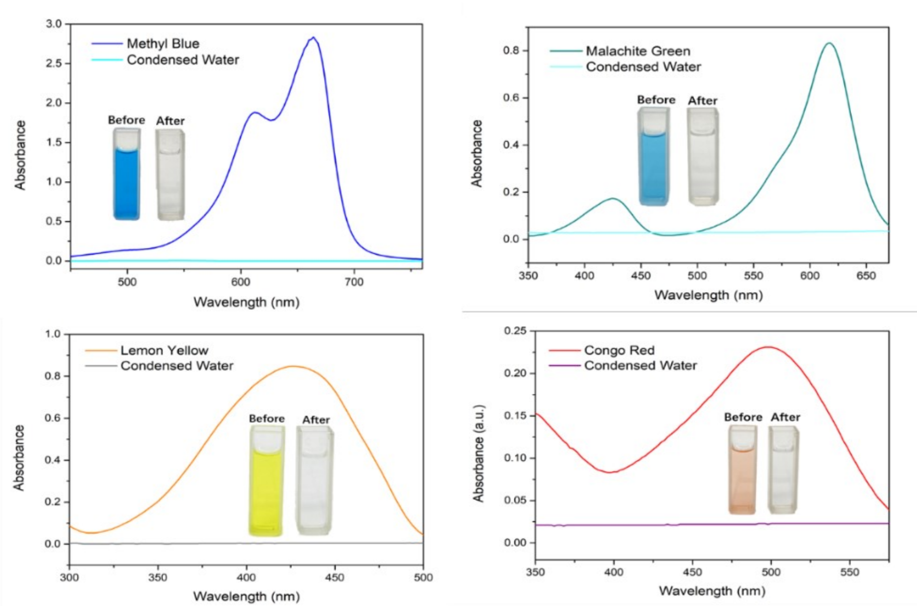

Fig. S14. UV-visible absorbance of different kinds of organic dyes in water before and after treatment.

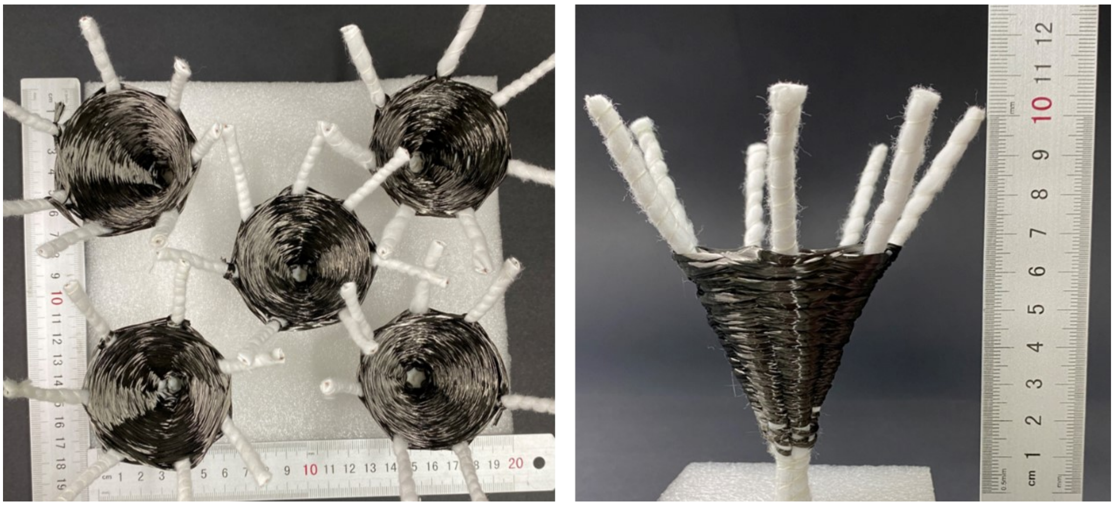

Fig. S15. Optical images of an array of 3D CFC-Cone-7 evaporators.

Table S2. The comparison of costs and evaporation rates of different evaporators.

Photothermal Materials	Cost (US Dollar m^{-2})	Evaporation rate ($kg\ m^{-2}\ h^{-1}$)	Reference
GO/ $FeCl_3$ Ni foam	124.07	1.6	[6]
MOF/Copper mesh	190	1.5	[7]
GO-CNTs filter paper	36.97	1.59	[8]
TiO_2/ PVA hydrogel	293.21	3.6	[9]
GO filer paper/ PS foam	20.0	1.45	[10]
PPy stainless steel mesh	55	0.92	[11]
PPy paper	20	1.35	[12]
GO-PTFE mold filter paper	16.7	1.62	[13]
rGO-agarose Cellulose sponge	14.38	1.56	[14]
Biomass mesoporous carbon composite	39	1.58	[15]
PPy cellulose fabric	3	0.6	[16]
Carbon fibre-cotton	8	3.27	Our work

Supplementary References

[1] Y. Wang, C. Wang, X. Song, M. Huang, S. K. Megarajan, S. F. Shaukat, H. Jiang, *J. Mater. Chem. A.*, 2018, **6**, 9874.

[2] S. Chaule, J. Hwang, S. J. Ha, J. Kang, J. C. Yoon, J. H. Jang, *Adv. Mater.*, 2021, **33**, 2102649.

[3] L. Q. Liu, X. L. Wang, M. Jing, S. G. Zhang, G. Y. Zhang, S. X. Dou, G. Wang, *Adv. Mater.,* 2012, **24**, 6318.

[4] R. Yu, K.-L. Ching, Q. Lin, S.-F. Leung, D. Arcrossito, Z. Fan, *ACS Nano,* 2011, **5**, 9291.

[5] T. Li, Q. Fang, J. Wang, H. Lin, Q. Han, P. Wang, F. Liu, *J. Mater. Chem. A.*, 2021, **9**, 390.

[6] H. Ren, M. Tang, B. Guan, K. Wang, J. Yang, F. Wang, M. Wang, J. Shan, Z. Chen, D. Wei, *Adv. Mater.,* 2017, **29**, 1702590.

[7] Q. Ma, P. Yin, M. Zhao, Z. Luo, Y. Huang, Q. He, Y. Yu, Z. Liu, Z. Hu, B. Chen, *Adv. Mater.,* 2019, **31**, 1808249.

[8] S. Hong, Y. Shi, R. Li, C. Zhang, Y. Jin, P. Wang, *ACS Appl. Mater. Interfaces,* **2018**, 10, 28517.

[9] Y. Guo, X. Zhou, F. Zhao, J. Bae, B. Rosenberger, G. Yu, *ACS Nano,* 2019, **13**, 7913.

[10] X. Li, W. Xu, M. Tang, L. Zhou, B. Zhu, S. Zhu, J. Zhu, *P. Natl. Acad. Sci.*, 2016, **113**, 13953.

[11] L. Zhang, B. Tang, J. Wu, R. Li, P. Wang, *Adv. Mater.,* 2015, **27**, 4889.

[12] X. Wang, Q. Liu, S. Wu, B. Xu, H. Xu, *Adv. Mate.,* 2019, **31**, 1807716.

[13] P. Zhang, J. Li, L. Lv, Y. Zhao, L. Qu, *ACS Nano,* 2017, **11**, 5087.

[14] Y. Wang, X. Wu, T. Gao, Y. Lu, X. Yang, G. Y. Chen, G. Owens, H. Xu, *Nano Energy,* 2021, **79**, 105477.

[15] F. Liu, B. Zhao, W. Wu, H. Yang, Y. Ning, Y. Lai, R. Bradley, *Adv. Funct. Mater.* 2018, **28**, 1803266.

[16] G. Ni, S. H. Zandavi, S. M. Javid, S. V. Boriskina, T. A. Coo*per, G. Chen, Energy Environ.Sci.,* 2018, **11**, 1510.